Combustion and Flame 290 (2026) 115085

Contents lists available at ScienceDirect

Combustion and Flame

journal homepage: www.sciencedirect.com/journal/combustion-and-flame

Modeling of soot oxidation in non-premixed turbulent flames under soot break-through conditions

Gandolfo Scialabba [a,*], Kai Niemietz [a], Antonio Attili [b], Heinz Pitsch [a]

[a] Institute for Combustion Technology, RWTH Aachen University, Aachen, 52056, Germany
[b] School of Engineering, Institute for Multiscale Thermofluids, University of Edinburgh, Edinburgh, EH9 3FD, United Kingdom

ARTICLE INFO

Keywords:
Soot
Soot oxidation
Soot break-through modeling
LES

ABSTRACT

Soot break-through in non-premixed turbulent flames, i.e., soot particles reaching fuel-lean regions without being fully oxidized, occurs when sufficiently fast soot particle drift is paired with local flame extinction. Accurate modeling of this phenomenon is therefore essential for reliable predictions of global soot emissions. Consequently, reduced-order models for soot oxidation must account for local extinction and reignition to capture potential soot break-through. In this work, the soot break-through prediction capabilities of existing Large-Eddy Simulation (LES) subfilter-scale models are systematically assessed. The impact of different soot subfilter-scale models on soot oxidation and break-through is compared to that obtained with the Statistically Most Likely Distribution (SMLD) model, a presumed PDF model specifically designed to improve local extinction prediction. An *a priori* evaluation, using available Direct Numerical Simulation data designed to obtain strong levels of local extinction and soot break-through, has shown that the SMLD model improves predictions of the filtered soot oxidation rate under soot break-through conditions, compared to the other considered models. In particular, the SMLD model significantly improves the soot oxidation predictions in lean regions, i.e., below stoichiometric mixture fractions, where additional oxidation events are observed due to either local partial extinction or reignition. Further assessment is performed in LES of a swirl-stabilized model aero-engine combustor, including *a posteriori* evaluation, where the applicability of the SMLD model in capturing soot break-through events is demonstrated.

Novelty and significance statement This study presents a novel and fundamental systematic assessment of presumed-PDF models for predicting soot oxidation rates under soot break-through conditions. Soot LES subfilter-scale models are evaluated, for the first time, against Direct Numerical Simulation data featuring significant local extinction and soot break-through. Additionally, an existing presumed PDF model, originally developed to improve predictions of local extinction and reignition, is applied here to soot oxidation, showing good performance under soot break-through-relevant conditions. Its applicability is further demonstrated in a model aero-engine combustor. Because turbulence-chemistry-soot interactions remain an open challenge in combustion modeling, improving soot evolution predictions and reliably capturing soot break-through events represent an important step toward the development of cleaner, low-emission combustion systems.

1. Introduction

To meet the increasingly stringent regulatory limits, achieving lower soot emissions is crucial for the development of next-generation combustion technologies. The modeling of soot formation and evolution remains a challenging task in combustion science due to its inherent complexity. This complexity stems from various phenomena such as the intricate gas-phase chemistry of polycyclic aromatic hydrocarbons (PAHs) and incipient soot particle formation, the subsequent aerosol dynamics, and the wide range of time scales from slow formation and growth to fast oxidation, all characterized by strong nonlinearities. Additionally, in practical combustion applications, soot particles and agglomerates are often exposed to turbulent flows, leading to further convoluted nonlinear turbulence-chemistry-soot interactions, whose accurate modeling is crucial to capture soot particle formation and evolution [1].

In non-premixed turbulent flames, the effects of turbulent stirring and unsteady effects on soot particulate formation, growth, and consumption have been widely investigated, both numerically [2–7] and experimentally [8,9]. Previous direct numerical simulation (DNS)

* Corresponding author.
E-mail address: g.scialabba@itv.rwth-aachen.de (G. Scialabba).

https://doi.org/10.1016/j.combustflame.2026.115085
Received 5 March 2026; Received in revised form 24 May 2026; Accepted 24 May 2026
Available online 31 May 2026
0010-2180/© 2026 The Authors. Published by Elsevier Inc. on behalf of The Combustion Institute. This is an open access article under the CC BY license (http://creativecommons.org/licenses/by/4.0/).

studies [4] showed that, under turbulent conditions, soot is rapidly advected from the particle inception and growth regions, hindering soot growth, due to the slower PAH and soot formation chemistry. Conversely, larger residence times, typical of flow regions with low scalar dissipation rates such as inside large vortices, significantly favor soot formation, consistent with laminar counterflow experimental studies [10], due to the relatively long time scales of soot formation and growth. Moreover, due to the high Schmidt number (ratio of momentum and mass diffusivities, $\mathrm{Sc} = \nu/D$) characteristic of aerosols, typically, no significant diffusive transport is observed for soot [3]. When soot volume fraction and number density fields are exposed to turbulent flows, a strong intermittency is observed, and their distribution is partially decoupled from the gaseous mixture field [4]. Furthermore, Attili et al. [5] showed that soot formation, growth, and spatial distribution are also impacted by variations of the Damköhler number, which is defined as the ratio of flow and chemical time scales. In their parametric variation study, a lower Damköhler number, which translates into higher scalar dissipation rates, was found to hinder PAH formation and soot mass growth rates.

Soot particle consumption due to surface oxidation reactions is significantly faster than soot particle inception and growth. Therefore, strong interactions of soot oxidation and turbulence occur, due to their comparable time scales [6,7]. Local flame extinction is observed under highly strained conditions [11], which, combined with strong advection of soot [3], can lead to soot emission as a result of a partial or complete lack of oxidation. This "soot break-through" has been reported both experimentally [9] and numerically [2,5]. Extinction may be driven by heat loss from soot radiation in large fires [12,13], but in technical combustion applications, such as aero-engines, soot residence times are more limited and strain-induced extinction is the governing mechanism.

Previously, a first comprehensive DNS study on soot break-through has been carried out by the authors [6]. Three turbulent non-premixed temporal jet flames with different levels of local flame extinctions were analyzed. The different flame extinction levels were obtained by a Damköhler number variation at fixed Reynolds number, with a clear increase in soot break-through levels for the lowest Damköhler number case, due to the larger and more frequent extinction regions observed. Soot break-through is driven primarily by extinction, which in non-premixed flames is characterized by large mixture fraction dissipation rates (χ_Z)

$$\chi_Z = 2D_Z \left(\frac{\partial Z}{\partial x_i} \right)^2 , \tag{1}$$

and fast soot advection due to turbulent stirring, which is linked to the relative drift of soot with respect to the mixture fraction and can be quantified through the mixture fraction diffusion rate (ξ_Z)

$$\xi_Z = \frac{1}{\rho} \frac{\partial}{\partial x_i} \left(\rho D_Z \frac{\partial Z}{\partial x_i} \right) , \tag{2}$$

with ρ, Z, and D_Z being the density, mixture fraction, and mixture fraction diffusivity. The DNS study also showed that, due to local partial extinction and reignition, soot oxidation can occur below the stoichiometric mixture fraction, as some of the soot crossing an extinguished oxidation layer can be oxidized at a later stage.

To further explore the impact of the soot oxidation reaction time scales on soot break-through, the DNS dataset has been extended with a parametric variation of the lowest Damköhler case (highest soot break-through levels) [7]. Five additional DNSs were performed, in which both the OH and O_2 soot oxidation rate coefficients ($k_{\mathrm{Ox,OH}}$ and $k_{\mathrm{Ox,O_2}}$) were varied across up to three orders of magnitude while keeping everything else constant. Although a modest change in peak soot mass and soot number density was observed, the overall impact on soot break-through was minimal, as almost all soot patches found in leaner regions had crossed flame regions with strong local extinction, i.e., no oxidation. This implies that soot oxidation is fast and, as long as the flame is burning, the process is almost independent of the exact soot oxidation rates. The leading-order influence on the prediction of soot break-through and oxidation events in leaner regions is an accurate description of local flame extinction. Therefore, in reduced-order models such as for Large-Eddy Simulations (LES), it is crucial to model flame extinction to capture possible soot break-through events.

In LES, the small-scale interactions between soot and turbulence remain unresolved, also due to the highly intermittent distribution of soot at the subfilter scale. To this end, Mueller and Pitsch [14] developed an LES model in which the soot subfilter probability density function (PDF) is presumed to be a double-delta distribution with a sooting mode and a non-sooting mode, to better capture the large spatial intermittency of soot. Due to the disparate time scale between the evolution of the thermochemical state and soot, the model from Mueller and Pitsch assumes that the conditional soot and gas-phase distribution can be replaced with their corresponding marginal distributions [15]. This implies that soot and mixture fraction are independent, which, for slower processes such as PAH formation, soot inception, and soot growth, can be reasonably assumed. However, soot oxidation time scales are often comparable to those of the gas-phase, suggesting the need for an explicit modeling of the joint subfilter PDF of soot and the thermochemical state. Based on this observation, Yang et al. [16] proposed a new model in which the distribution of soot with respect to mixture fraction is explicitly included. Their proposed conditional soot subfilter PDF assumes soot to be confined in fuel-rich regions, where soot surface growth is faster than soot oxidation. To account for this, the model introduces a sharp cut-off mixture fraction value below which soot is no longer oxidized, assuming that soot oxidation is infinitely fast compared to the turbulent transport of soot. Later, to relax this assumption of an infinitely fast oxidation, Maldonado Colmán et al. [17], extended this model to account for finite-rate oxidation events, replacing the sharp cut-off mixture fraction limit with a smoother function dependent also on the relative motion of soot in the mixture fraction field. These models were found to improve soot oxidation predictions by reducing the spurious excessive oxidation both in *a priori* and *a posteriori* validations, compared to the original 2δ model from Mueller and Pitsch. Both models still imply that soot oxidation is strictly dependent on the location of soot in the mixture fraction space. However, as shown in the previous DNS work on soot break-through [6], soot oxidation can also be found below stoichiometric conditions due to local extinction and reignitions, and hence soot break-through.

In this work, different subfilter modeling approaches for soot oxidation are evaluated. Ihme and Pitsch [18,19] suggested a model extension to the Flamelet Progress Variable (FPV) model [20] to capture local extinction and reignition. In their model, an additional presumed PDF referred to as "Statistically Most Likely Distribution" (SMLD) for the reaction progress parameter is included, with a substantial improvement on the prediction of local flame extinction and reignition when used for LES of the high Reynolds Sandia Flames D and E [21]. Given the strong link between soot break-through and extinction, as evinced in the mentioned DNS studies [6,7], the main focus of this work is the modeling of soot oxidation in non-premixed flames under soot break-through conditions. To this end, the SMLD presumed PDF model is employed here for the first time to model soot oxidation rates in LES. The model is compared to the classical FPV model, typically used in LES, coupled with the above-mentioned state-of-the-art soot subfilter models [15–17].

This paper is structured as follows. First, the different formulations of the subfilter models used in the comparison are provided. Then, the models are tested *a priori* against DNS data characterized by strong local extinctions and soot break-through. In Section 4, the models are employed in an LES of a swirl-stabilized model aero-engine combustor for an *a posteriori* evaluation. Finally, concluding remarks are offered.

2. Numerical methods and models

2.1. Soot description

The soot particle size distribution evolution is described by the Population Balance Equation (PBE), which describes the spatial and temporal evolution of the Number Density Function (NDF). In LES, a direct solution of the PBE is unfeasible, and a commonly used approach is to describe soot statistically using a moment method [22]. To account for the fractal morphology of soot [23], a multivariate formulation for the description of soot particles and aggregates is employed. The used formulation, including their volume (V) and surface area (S) as described by Mueller et al. [24], is

$$M_{x,y} = \sum_{j=0}^{\infty} V_j^x S_j^y N_j \,, \tag{3}$$

where V_j, S_j, and N_j are the volume, surface, and particle number density of soot aggregates of class j, with x and y indicating the moment orders for volume and surface, respectively. The evolution of the set of statistical moments is described by

$$\frac{\partial M_{x,y}}{\partial t} + \frac{\partial u_i M_{x,y}}{\partial x_i} = \dot{M}_{x,y} \,, \tag{4}$$

where $\dot{M}_{x,y}$ is a source term containing the various particle internal processes: soot particle inception, surface growth by hydrogen abstraction and acetylene addition (HACA) [25], PAH adsorption, coagulation, and particle oxidation due to surface reactions. Diffusive transport is neglected in this work, due to the high Schmidt number characteristic of soot [3]. Thermophoretic transport [26] is also neglected as its contribution is negligible in turbulent non-premixed sooting flames [2,3]. A closure approach is required for the source term of the statistical moments, as they depend on additional unknown moments. Here, the Hybrid Method of Moments (HMOM) [27] is chosen. Four statistical moments, $M_{0,0}$, $M_{1,0}$, $M_{0,1}$, and N_0, are used for Eq. (4), with the last term describing the weight of a delta function representing the number of smallest particles at inception size [27]. The detailed expression for all the soot source terms can be found in Refs. [15,24,27], together with their derivation for the HMOM closure approach. The soot oxidation source term for a generic bivariate soot statistical moment $M_{x,y}$ is defined as follows

$$\dot{M}_{x,y}^{\mathrm{Ox}} = -\underbrace{\left(k_{\mathrm{Ox,OH}} + k_{\mathrm{Ox,O_2}}\right)}_{\text{Gas-phase}} \cdot \underbrace{\chi \left[\frac{\delta V}{V_0} {V_0}^x {S_0}^{y+1} N_0 + \sum_{i=1}^{\infty} \left(x\frac{\delta V}{V_i} + y\frac{\delta S}{S_i}\right) {V_i}^x {S_i}^{y+1} N_i\right]}_{\text{Soot}} \,, \tag{5}$$

where χ is the number of active sites per unit area that is assumed constant, i.e., $\chi = 1.7 \times 10^{19}$ m^{-2}, δV is the volume change, and δS is the corresponding change in surface [24,28]. The rate of oxidation by OH is modeled considering the collision rate between soot particles and OH radicals, where a constant collision efficiency of 0.13, as suggested by Neoh et al. [29], is employed. The corresponding soot OH oxidation rate coefficient $k_{\mathrm{Ox,OH}}$ is proportional to the OH concentration and the square root of temperature. Oxidation by O_2 is assumed to occur at radical sites on the particles' surface. As for the employed HACA model, the radical sites are modeled as being in a quasi-steady state [30]. The resulting expression for the soot O_2 oxidation rate coefficient $k_{\mathrm{Ox,O_2}}$ is dependent on the temperature and concentration of various abstracting radicals, and the corresponding stable species. The O_2 oxidation kinetic rate parameters from Kazakov et al. [31] are used. For $M_{1,0}$, which describes the total soot volume and which will be discussed in the following, Eq. (5) simplifies to

$$\dot{M}_{1,0}^{\mathrm{Ox}} = -\underbrace{\left(k_{\mathrm{Ox,OH}} + k_{\mathrm{Ox,O_2}}\right)}_{\text{Gas-phase}} \cdot \underbrace{\chi \cdot \delta V \cdot M_{0,1}}_{\text{Soot}} \,. \tag{6}$$

Such soot oxidation kinetics are consistent with various DNS and LES studies [4,6,14], and previous work has demonstrated that soot breakthrough is only marginally sensitive to variations in soot oxidation reaction time scales [7]. Therefore, the employed soot oxidation model is considered adequate for the present study.

2.2. Soot subfilter modeling

In LES, when the spatial filtering operation $\overline{(\cdot)}$ is applied to Eq. (4), the resulting filtered source term $\overline{\dot{M}_{x,y}}$ remains unclosed and requires modeling. The filtered source term is usually closed through convolution with a density-weighted PDF. For a generic source term, this is

$$\overline{\dot{M}_j} = \bar{\rho} \iint \frac{1}{\rho} \dot{M}(\psi_i, M_j) \widetilde{P}(\psi_i, M_j) \mathrm{d}\psi_i \mathrm{d}M_j \,, \tag{7}$$

where ψ_i is the set of thermochemical variables, M_j is the set of used soot moments, and $\widetilde{P}(\psi_i, M_j)$ is the joint subfilter PDF which must be modeled, either by transport or with a presumed PDF approach [32]. The second approach is considered here. Using Bayes' theorem, the joint PDF is expressed as

$$\widetilde{P}(\psi_i, M_j) = \widetilde{P}(\psi_i) P(M_j|\psi_i) \,, \tag{8}$$

with $\widetilde{P}(\psi_i)$ being dependent only on the gas-phase. The thermochemical state is typically modeled using the FPV model from Pierce and Moin [20], which is described in more detail in Section 2.3.1.

2.2.1. Marginal soot subfilter PDF

The second term of Eq. (8) is the soot moment subfilter PDF conditioned on the thermochemical quantities. According to Mueller and Pitsch [15], the conditional subfilter PDF can be simplified to a marginal PDF of only the soot scalars

$$P(M_j|\psi_i) \approx P(M_j) \,, \tag{9}$$

if soot and thermochemical time scales are significantly different—an assumption valid for the slower processes such as formation and growth. For the modeling of the marginal soot PDF, due to the large spatial intermittency of soot, Mueller and Pitsch proposed a presumed PDF with two delta distributions, for a sooting and non-sooting mode, respectively

$$P(M_j) = \omega\delta(M_j) + (1-\omega)\delta(M_j - M_j^*) \,, \tag{10}$$

where ω is the subfilter intermittency and M_j^* is formulated to recover the filtered values of the soot scalars $\overline{M_j}$ upon convolution with $\widetilde{P}(\psi_i, M_j)$. The subfilter intermittency can be defined as $\omega = 1 - \overline{M_{0.0}}^2 / \overline{M_{0,0}^2}$, and represents the probability of not finding soot within an LES filter. To estimate ω, an additional transport equation for $\overline{M_{0,0}^2}$ must be solved. Further details on the 2δ model formulation can be found in Refs. [14,15]. Starting from Eq. (7), and using Eq. (5) and (10), the generic filtered soot oxidation source term can be written as

$$\begin{aligned}
\overline{\dot{M}_j^{\mathrm{Ox}}} &= -\bar{\rho} \iint \frac{1}{\rho} k_{\mathrm{Ox}}(\psi_i) f(M_j) \widetilde{P}(\psi_i) P(M_j) \mathrm{d}\psi_i \mathrm{d}M_j \\
&= -\left[\bar{\rho} \int \frac{1}{\rho} k_{\mathrm{Ox}}(\psi_i) \widetilde{P}(\psi_i) \mathrm{d}\psi_i\right] \left[(1-\omega) f(M_j^*)\right] \\
&= -\widetilde{k}_{\mathrm{Ox}}^{\mathrm{FPV}} \left[\frac{\overline{M_{0.0}}^2}{\overline{M_{0,0}^2}} f(M_j^*)\right] \,,
\end{aligned} \tag{11}$$

where $\widetilde{k}_{\mathrm{Ox}}^{\mathrm{FPV}}$ indicates the sum of both O_2 and OH oxidation constants, and it includes, for simplicity, all constant values from Eq. (5) and the result of convolution using the FPV model from Pierce and Moin [20]. In the following, this model will be referred to as either the Marginal PDF model or simply the FPV model.

2.2.2. Conditional soot subfilter PDF

Soot oxidation time scales are known to be of the same order of magnitude as the main heat-releasing chemistry, especially for surface reactions with OH [33]. Therefore, the assumption of soot evolution processes being slow compared to the main heat-release chemistry is no longer valid for oxidation processes.

To account for the relative location of soot in mixture fraction space, a different approach for modeling the soot moment subfilter conditional PDF ($P(M_j|\psi_i)$) in Eq. (8) has been proposed by Yang et al. [16] for non-smoking flames. In their model, which will be referred to as the "Infinitely Fast Oxidation" (IFO) model, the conditional subfilter PDF includes a mixture fraction dependency, where the sooting mode is activated only for mixture fraction values larger than a given cut-off value Z_{soot}. This dependency is modeled using an Heaviside function

$$\mathcal{G}_{\text{IFO}}(Z,\chi_{st}) = H(Z - Z_{\text{soot}}(\chi_{st})), \tag{12}$$

where the cut-off mixture fraction varies with the reference mixture fraction dissipation rate χ_{st}. The cut-off value $Z_{\text{soot}}(\chi_{st})$ is taken as the mixture fraction value at which soot surface growth and soot oxidation are equal. The model implies that soot oxidation, for non-smoking flames, is so fast that soot is oxidized before reaching any mixture fraction value below the imposed cut-off. This assumption holds for non-smoking flames, and it has been shown to reduce spurious large oxidation, especially for large filter sizes. However, the IFO formulation was later relaxed by Maldonado Colmán et al. [17] to account for finite-rate soot oxidation events where soot might penetrate further into leaner mixtures or remains unoxidized. In their model, the cut-off value definition is retained, but the Heaviside function is replaced by a smoother hyperbolic tangent function

$$\mathcal{G}_{\text{FRO}}(Z,\chi_{st}) = \frac{1}{2} + \frac{1}{2}\tanh\left(\frac{Z - (Z_{\text{soot}} + \delta_Z/2)}{\delta_Z/2}\right), \tag{13}$$

where the mixture fraction distance $\delta_Z = \xi_Z/k_{\text{Ox}}$ determines how far soot is transported in the mixture fraction space before it is completely oxidized, and is evaluated at $Z = Z_{\text{soot}}$. The model will be referred to as the "Finite-Rate Oxidation" (FRO) model. The detailed formulation of the IFO and FRO models can be found in Refs. [16,17], and only a brief description is provided in the following. Introducing the IFO/FRO models, the conditional PDF in Eq. (8) becomes

$$P(M_j|\psi_i) = \omega\delta(M_j) + (1-\omega_Z)\delta(M_j - M_j^*(Z,\chi_{st})), \tag{14}$$

with $M_j^*(Z,\chi_{st}) = M_j^{**}\mathcal{G}(Z,\chi_{st})$, where $\mathcal{G}$ indicates either the IFO or FRO model, and M_j^{**} is formulated, as for the marginal PDF model, to recover $\overline{M_j}$ upon convolution with the joint subfilter PDF. The subfilter intermittency ω_Z is then defined as

$$\omega_Z = 1 - \frac{1}{\int \mathcal{G}(Z,\chi_{st})\widetilde{P}(Z)\mathrm{d}Z} \cdot \frac{\overline{M_{0,0}}^2}{\overline{M_{0,0}^2}}. \tag{15}$$

Applying this presumed PDF model and definition of the subfilter intermittency ω_Z to the filtered soot oxidation source term (Eqs. (5) and (7)), it follows

$$\begin{aligned}\overline{M_j^{\text{Ox}}} &= -\bar{\rho}\iint \frac{1}{\rho}k_{\text{Ox}}(\psi_i)f(M_j)\widetilde{P}(\psi_i)P(M_j|\psi_i)\mathrm{d}\psi_i\mathrm{d}M_j \\ &= -\left[\frac{\bar{\rho}\int \frac{1}{\rho}k_{\text{Ox}}(\psi_i)\mathcal{G}(Z,\chi_{st})\widetilde{P}(\psi_i)\mathrm{d}\psi_i}{\int \mathcal{G}(Z,\chi_{st})\widetilde{P}(\psi_i)\mathrm{d}\psi_i}\right]\left[\frac{\overline{M_{0,0}}^2}{\overline{M_{0,0}^2}}f(M_j^{**})\right] \\ &= -\widetilde{k}_{\text{Ox}}^{\text{IFO/FRO}}\left[\frac{\overline{M_{0,0}}^2}{\overline{M_{0,0}^2}}f(M_j^{**})\right],\end{aligned} \tag{16}$$

where $\widetilde{k}_{\text{Ox}}^{\text{IFO/FRO}}$ is the soot oxidation constant k_{Ox} including the effects of convolution with either the IFO or the FRO (Eq. (14) coupled with either Eq. (12) or (13)) conditional PDF model and the FPV model. All quantities necessary for their computation, such as Z_{soot} and δ_Z, can be determined solely from the gas-phase chemistry. Therefore, the IFO/FRO soot oxidation coefficients can be precomputed and stored in a database in the same way as for the marginal PDF model, thus requiring no major modifications for their implementation [16,17]. The same conditional PDF model must be applied to the HACA surface growth, since otherwise HACA growth would not be counteracted in the regions where soot oxidation is neglected. In the following, both the IFO and FRO models are combined exclusively with the FPV model.

2.3. Turbulent combustion model

In this section, the employed combustion models are described. First, in Section 2.3.1, the FPV model formulation from Pierce and Moin [20] is given. Then, in Section 2.3.2, the model extension from Ihme and Pitsch [18,19] to account for extinction and reignition phenomena is provided.

2.3.1. Flamelet progress variable approach

In the FPV model from Pierce and Moin [20] for non-premixed turbulent flames, the local thermochemical equation of state is obtained by solving steady flamelet equations [34], which are parametrized by the mixture fraction Z and a reaction progress parameter Λ, the latter identifying each flamelet solution, as $\psi = \mathcal{F}(Z,\Lambda)$. The presumed PDF for the thermochemical quantities $\widetilde{P}(\psi_i)$, assuming independence between Z and Λ [20], is

$$\widetilde{P}(\psi_i) = \widetilde{P}(Z,\Lambda) = \frac{\bar{\rho}}{\rho}\widetilde{P}(Z)\widetilde{P}(\Lambda). \tag{17}$$

Among the different choices for the presumed PDF of the mixture fraction, the beta distribution ($\widetilde{P}(Z) = \beta(Z;\widetilde{Z},\widetilde{Z''^2})$) is widely used for describing the passive scalar subgrid-scale distribution [11,35]. In the model of Pierce and Moin [20], the subfilter states in a computational cell are represented by a single flamelet, which is described by a delta distribution

$$\widetilde{P}(\Lambda) = \delta(\Lambda - \widetilde{\Lambda}). \tag{18}$$

The reaction progress parameter Λ is usually defined through a reaction progress variable C, typically defined as a linear combination of major reaction product mass fractions, here taken as $C = Y_{\text{H}_2\text{O}} + Y_{\text{CO}_2} + Y_{\text{CO}} + Y_{\text{H}_2}$ and, with one possible choice being its value at stoichiometric conditions $\Lambda = C|Z_{st} = C_{st}$. Assuming a bijective relation $\Lambda = \mathcal{F}_C^{-1}(Z,C)$, the Λ dependency can be eliminated, and a generic thermochemical variable $\widetilde{\phi}$ in the FPV model can be expressed as function of Z and C only

$$\widetilde{\phi}^{\text{FPV}} = \widetilde{\mathcal{G}}_\phi(\widetilde{Z},\widetilde{Z''^2},\widetilde{C}). \tag{19}$$

A more detailed description of the FPV model can be found in Ref. [20].

2.3.2. Statistically most likely distribution

The description of the thermochemical state within a computational cell by a single flamelet (as with FPV) is often sufficient in the case of strongly burning flames. However, it has been shown that the convolution of multiple flamelets (i.e., the use of higher moment information for the progress variable) significantly improves local extinction and reignition predictions [36]. To this end, Ihme and Pitsch [18,19] employed a presumed PDF approach, known as Statistically Most Likely Distribution (SMLD), based on the formulation from Pope [37], in which higher moment information for the progress reaction parameter Λ ($\Lambda = C|Z_{st}$) is included. The detailed description of the SMLD model is omitted here for brevity and can be found in Refs. [18,19], with only the key features being described in the following. In the SMLD model, the delta distribution for Λ (Eq. (18)) is replaced by a presumed PDF which uses higher order statistics of Λ. Then, the presumed PDF using the second-order moment of the progress variable is

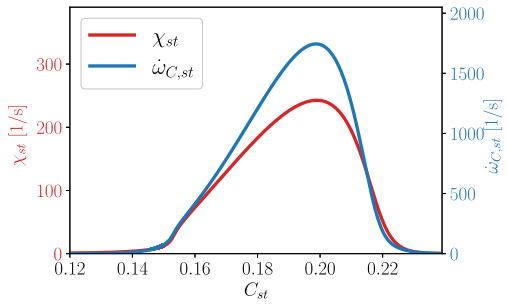


Fig. 1. $\dot{\omega}_{C,st}$ and χ_{st} as a function of $\Lambda = C_{st}$ from the flamelet table computed with flamelets with the same fuel/oxidizer composition as used in the DNS.

$$\widetilde{P}_{\mathrm{SML},2}(\Lambda) = \frac{1}{\sqrt{\widetilde{C''^2}}}\left[1+\left(\frac{\dot{\omega}_{C,st}(\Lambda)\gamma_C\widetilde{Z''^2}}{\chi_{Z,st}(\Lambda)\sqrt{\widetilde{C''^2}}}\right)^2\right]^{-1/2} \cdot \exp\left(\sum_{i=0}^{2} a_i \Lambda^i\right), \tag{20}$$

where $\dot{\omega}_{C,st}(\Lambda)$ and $\chi_{Z,st}(\Lambda)$ are the progress variable source term and the mixture fraction dissipation rate at stoichiometric conditions, as function of the progress reaction parameter Λ (i.e., for a given flamelet), γ_C is a time scale ratio which, for simplicity, is set to 1, and a_i are a set of Lagrangian multipliers which must be precomputed for each combination of $[\widetilde{Z}, \widetilde{C}, \widetilde{Z''^2}, \widetilde{C''^2}]$ imposing the constraints for each of the considered moments of C. The ratio between $\dot{\omega}_{C,st}(\Lambda)$ and $\chi_{Z,st}(\Lambda)$ expresses the ratio between a reaction time scale $\dot{\omega}_{C,st}$ and a mixing time scale $\chi_{Z,st}$ (shown in Fig. 1), thus influencing the presumed PDF shape when mixing and reaction have comparable time scales (e.g., strong mixing leading to local extinction).

The Lagrangian multipliers a_i can be precomputed solely as a function of Z and C; thus, as for the FPV model, no direct information about the moments of the reaction progress parameter is required:

$$\begin{aligned}\widetilde{\phi}^{\mathrm{SMLD}} &= \widetilde{\mathcal{G}}_\phi(\widetilde{Z}, \widetilde{Z''^2}, \widetilde{C}, \widetilde{C''^2}) \\ &= \bar{\rho}\iint \frac{1}{\rho}\mathcal{F}_\phi(Z,\Lambda)\beta(Z;\widetilde{Z},\widetilde{Z''^2}) \\ &\cdot \widetilde{P}_{\mathrm{SML},2}(\Lambda;\mathbf{a}(\widetilde{Z},\widetilde{C},\widetilde{Z''^2},\widetilde{C''^2}))\mathrm{d}Z\mathrm{d}\Lambda\,.\end{aligned} \tag{21}$$

Using both the marginal soot PDF (Eq. (10)) and the SMLD model (Eq. (21)) for k_{Ox}, the soot oxidation source term becomes

$$\overline{\dot{M}_j^{\mathrm{Ox}}} = -\widetilde{k}_{\mathrm{Ox}}^{\mathrm{SMLD}}\left[\frac{\overline{M_{0,0}}^2}{\overline{M_{0,0}^2}} f(M_j^*)\right], \tag{22}$$

similar to Eq. (11).

3. *A priori* analysis on DNS data with soot break-through

3.1. DNS database

For the *a priori* testing of the soot oxidation models, the temporally evolving non-premixed hydrocarbon/air jet flame from a previous study of the authors [6] is considered. In this dataset, different levels of soot break-through are obtained by varying the Damköhler number, leading to varying degrees of local extinctions. A 3D rendering of the DNS right after initialization and during the peak extinction and break-through phase is shown in Fig. 2. A 1-methylnaphthalene/ethylene/nitrogen (2/25.5/72.5 by volume) mixture is used for the fuel, which, compared to other studies [4], favors high levels of soot formation and growth at much earlier stages and allows the analysis of the later stages of soot evolution. For all cases, a jet Reynolds number of $\mathrm{Re} = 2U_c H/\nu \approx 20000$ is used. The case with the lowest Damköhler number is considered, where $H = 5$ mm is the fuel slab width, $U_c = 38.12$ m/s is the main jet velocity, and a grid spacing of $dx = 80\,\mu$m is used. A reduced 65-species kinetic model, derived from the detailed model by Langer et al. [38], is used, and soot is modeled as in Section 2.1. The DNS dataset, its initialization, the employed models, and the physical description of soot break-through are extensively described in Refs. [6,7]. In addition to the low Damköhler case discussed in Ref. [6], a DNS with equal diffusivities (Le = 1) was also computed and will be considered in the subsequent analysis, to remove any differential diffusion effect on the gas-phase [39] and allow the use of flamelets with equal diffusivities for the analysis. The analysis is performed on different snapshots of the DNS taken across the peak extinction and soot break-through phases (2 ms $< t_{\mathrm{DNS}} <$ 5 ms).

The different models introduced in Section 2 will be tested, using precomputed chemistry tables populated with non-premixed laminar flamelets as a function of the control variables Z and C. For the model comparison, the DNS source terms are replaced with the corresponding fields obtained from the chemistry table. These fields are mapped onto the fully resolved DNS data and are then filtered with a box filter of different sizes ($\Delta/dx = 4, 8, 16$) and used as the target data. This additional step simplifies the model comparison by isolating the effects of the presumed PDF models, removing any additional error introduced by the chemistry table parametrization when comparing directly with the actual filtered DNS data. In the following, only the results for $\Delta/dx = 8$ and $t_{\mathrm{DNS}} = 2.75$ ms (right image of Fig. 2) are shown. The results for other DNS snapshots and filter sizes are provided in Section 1.3 of the supplementary material.

3.2. Results

First, to assess the influence of the SMLD model on extinction and reignition, the source term of the progress variable $\dot{\omega}_C$ computed using the FPV ($\overline{\dot{\omega}}^{\mathrm{FPV}}$, Eq. (19)) and the SMLD ($\overline{\dot{\omega}}^{\mathrm{SMLD}}$, Eq. (21)) models are compared with the mapped filtered DNS value $\overline{\dot{\omega}(Z,C)}$. A visual comparison is provided by the instantaneous images in Fig. 3, where the SMLD model clearly shows superior agreement with the DNS in regions of moderate source term values due to local extinction and reignition.

Furthermore, the SMLD model effectively reduces the overpredictions observed with the classical FPV model, as also evidenced by the averaged values conditioned on $\widetilde{Z}$ (Fig. 4), showing the good applicability of the model under strong flame extinction [18]. The mapped filtered DNS data exhibits larger peak values than the actual filtered DNS. The discrepancy becomes larger as more reignition occurs. A more detailed comparison for different DNS snapshots, including soot oxidation-related quantities, is provided in Section 1.1. of the supplementary material. The mapping impact on the oxidation rate and constant is much less pronounced; thus, only the mapped DNS data will be shown for the remaining analysis.

In the following, a comparison of the filtered soot oxidation rates $\overline{\dot{M}_{1,0}^{\mathrm{Ox}}}$ is given. The mapped reference DNS data $\overline{\dot{M}_{1,0}^{\mathrm{Ox}}(Z,C)}$ is compared with the FPV (Eq. (11)), FPV-FRO (Eq. (16)), and SMLD (Eq. (22)) models. The original filtered DNS data is included for reference. For $M_{1,0}$, all the models can be expressed as

$$\overline{\dot{M}_{1,0}^{\mathrm{Ox}}} = -\widetilde{k}_{\mathrm{Ox}}^{\mathrm{model}} \cdot \overline{M_{0,1}}\,, \tag{23}$$

where $\widetilde{k}_{\mathrm{Ox}}^{\mathrm{model}}$ is the oxidation rate coefficient estimated with each of the three considered models. For this comparison, the IFO model is not considered, given the nature of the DNS data characterized by strong extinctions and soot break-through. A more conservative fixed cut-off value Z_{soot} set at stoichiometric conditions ($Z_{st} \approx 0.18$) is used for the FPV-FRO model in this section, as significant soot oxidation occurs near or below stoichiometry. The comparison between the FPV (marginal PDF) and the FPV-FRO (conditional PDF) models provides a direct estimation of the impact of the presumed PDF used for the soot part.

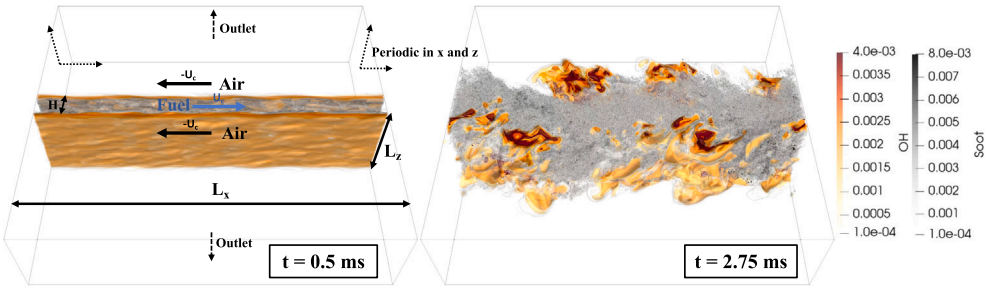


Fig. 2. OH and soot mass fraction fields visualization from reference DNS [6]. Left: OH profile and velocity arrangement with indicated boundary conditions after initialization ($t_{\mathrm{DNS}} = 0.5$ ms). Right: OH and soot mass fraction fields during the peak extinction and soot break-through phase ($t_{\mathrm{DNS}} = 2.75$ ms).

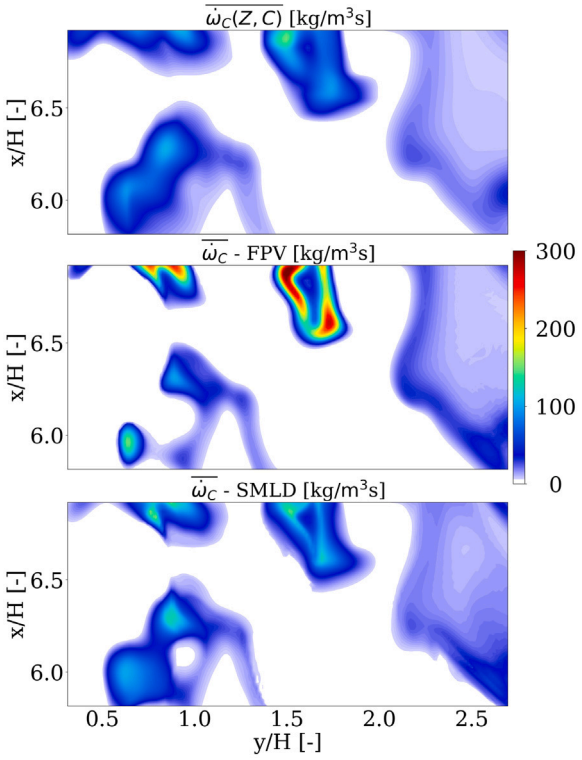


Fig. 3. $\overline{\dot{\omega}_C}$ comparison for $\Delta/dx = 8$. Top: DNS reference solution (fields mapped with Z and C before filtering). Mid: Flamelet Progress Variable (FPV) model. Bottom: Statistically Most Likely Distribution (SMLD) model.

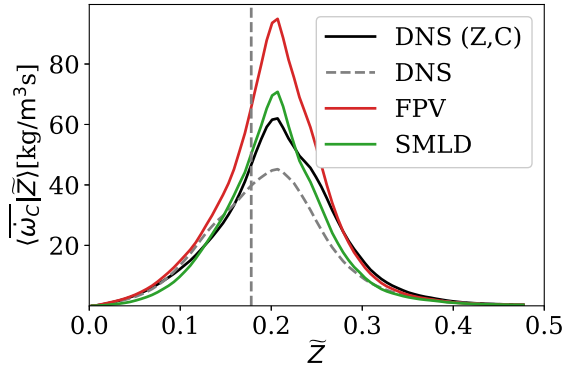


Fig. 4. $\overline{\dot{\omega}_C}$ conditioned on $\widetilde{Z}$ for the actual DNS data (dashed black), the reference mapped DNS data (solid black), Flamelet Progress Variable model (FPV, red), and Statistically Most Likely Distribution model (SMLD, green). Computed using filtered DNS data (Δ = 8dx) at $t_{\mathrm{DNS}} = 2.75$ ms, where peak extinction and soot break-through are observed.

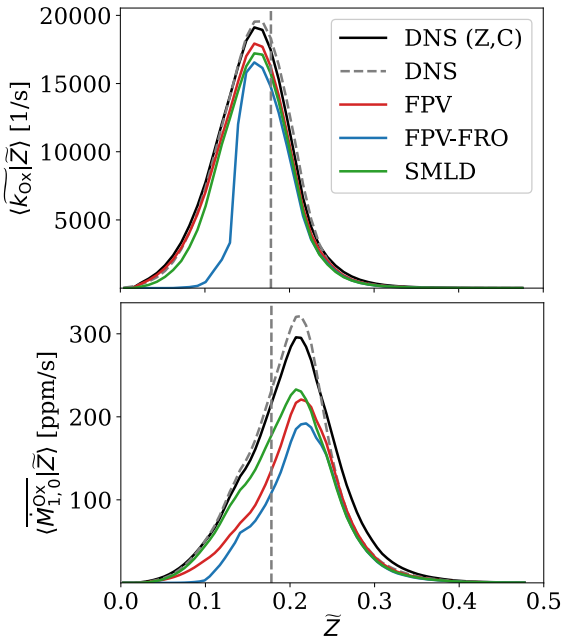


Fig. 5. $\widetilde{k}_{\mathrm{Ox}}$ (top) and $\overline{\dot{M}^{\mathrm{Ox}}_{1,0}}$ (bottom) conditioned on $\widetilde{Z}$ for reference mapped DNS data (DNS (Z,C)), filtered DNS data, Marginal PDF model (FPV), Finite Rate Oxidation (FPV-FRO) model, and Statistically Most Likely Distribution (SMLD) model. The vertical dashed line indicates Z_{st}.

The full results using both IFO and FRO models with a larger fixed cut-off value and the adaptive cut-off value $Z_{\mathrm{soot}}(\chi_{st}|k_{\mathrm{Ox}} = k_{\mathrm{Surf}})$ are provided in Section 1.4 of the supplementary material. No significant change in the FPV-FRO results is observed when using the adaptive cut-off value, except for a slight improvement for lean soot oxidation events with $Z_{\mathrm{soot}} = Z_{st}$.

In Fig. 5, the mean filtered soot oxidation rate constants ($\widetilde{k}_{\mathrm{Ox}}$) and source terms ($\overline{\dot{M}^{\mathrm{Ox}}_{1,0}}$) conditioned on $\widetilde{Z}$ are given. A small peak $\widetilde{k}_{\mathrm{Ox}}$ discrepancy is observed for all models, probably due to the effect of convolution with a presumed PDF. The reduction of the peak soot oxidation rate is more evident for all the cases. Since the models can all be expressed as in Eq. (23), the actual subfilter conditional PDF $P(M|\xi_i)$ is not explicitly considered (except for the cut-off value in the IFO/FRO models), leading to possible underprediction of strong soot oxidation layers, i.e., the subfilter soot/gas-phase distribution is limited to the imposed cut-off value rather than accounting for the actual relative soot location with respect to the oxidation layer. At the same time, complete soot oxidation it typically observed before reaching peak OH radical regions [6], thus a rate underprediction in the strong oxidation regions is not expected to significantly affect the overall smoke emissions. To further address this reduction, PDFs of the

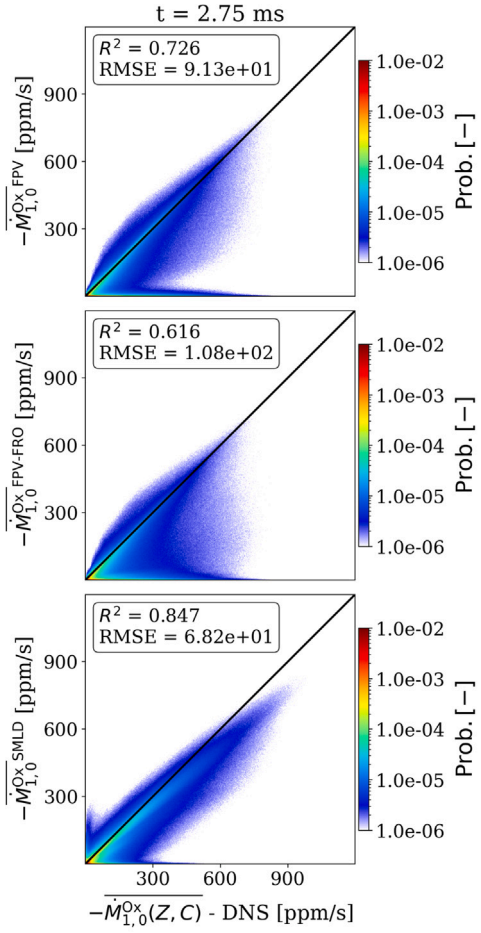


Fig. 6. Joint PDF of reference $\dot{M}^{Ox}_{1,0}$ and different models: FPV (top), Finite Rate Oxidation (FPV-FRO, center), and SMLD (bottom).

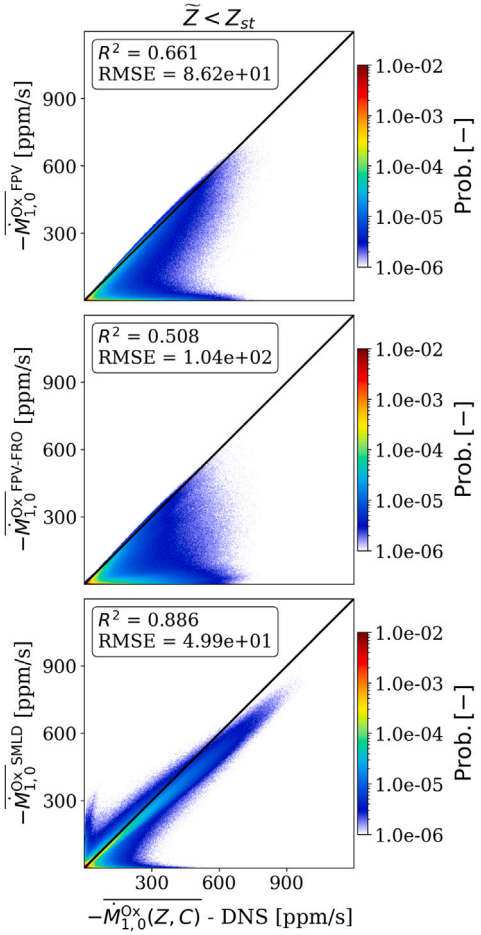


Fig. 7. Joint PDF comparison of $\dot{M}^{Ox}_{1,0}$ for the FPV, FPV-FRO, and SMLD models for data below stoichiometry ($\widetilde{Z} < Z_{st}$).

soot oxidation rates conditioned on different mixture fraction values are included in Section 1.2 of the supplementary material.

Among all models, the FPV-FRO model exhibits the largest deviation from DNS data, particularly near stoichiometric conditions, even when using a more conservative cut-off value (here, $Z_{soot} = Z_{st}$). In the limit of $Z_{soot} = 0$, the marginal PDF model is recovered, while larger cut-off values result in even lower oxidation levels. In the DNS data, a significant amount of oxidation occurs near and below stoichiometry due to the wide extinction regions and presence of soot in leaner regions [6]. The IFO/FRO models, by construction, assume less or no oxidation at and below the prescribed cut-off value and therefore cannot adequately capture such soot oxidation events, resulting in a further underprediction compared to the simple FPV model, which considers no conditional soot PDF. The FPV and SMLD models show comparable peak mean values above stoichiometric conditions, with some underprediction of the largest DNS levels. However, the SMLD model better captures the filtered DNS levels in the lean regions. Further comparisons are provided in the parity plots in Fig. 6, where both R^2 and RMSE are provided for FPV, FPV-FRO, and SMLD models. The smaller R^2 value for the FRO/DNS comparison clearly indicates the systematic underprediction of the DNS oxidation levels. Among the models, the smallest RMSE and an R^2 value closest to unity are observed for the SMLD model, due to improved predictions of oxidation rates in the lower range (0–300 ppm/s). To further evince the improved predictions of the SMLD model under break-through conditions, additional parity plots are shown in Fig. 7. Here, only points in the lean regions ($\widetilde{Z} < Z_{st}$) are considered. The FPV model fails to predict smaller oxidation events originating from unsteady extinction and reignition effects, yielding near-zero values in regions where the DNS data shows significant oxidation. In contrast, the SMLD model exhibits significantly better agreement, with data distributed much closer to the diagonal ($R^2 \approx 0.89$) and almost 50% reduction in RMSE.

4. *A posteriori* evaluation: LES of DLR model combustor

4.1. Combustor configuration and numerical framework

For the *a posteriori* evaluation of the different subfilter models discussed in Sections 2 and 3, the DLR ethylene/air high-pressure combustor investigated by Geigle et al. [40] is considered. This model swirl combustor is part of the International Sooting Flame workshop target flames [41] and has been investigated in several numerical studies [42–46]. A computational grid with 12 million cells is employed. A grid-independence study for the considered grid was carried out in previous LES studies by Chong et al. [44,46], demonstrating adequate resolution.

Two-dimensional slices of the computational domain and the instantaneous mixture fraction field are included in Fig. 8. The combustor chamber has a square cross section of 68 × 68 mm^2 and a height of 120 mm. Ethylene is injected between the two concentric air inlets through 60 straight channels (0.5 × 0.4 mm^2), at the location indicated in the figure. Four secondary dilution jets are located at the corners of the burner, further downstream, to mimic the secondary oxidation air stream of a Rich-Quench-Lean (RQL) aircraft combustor.

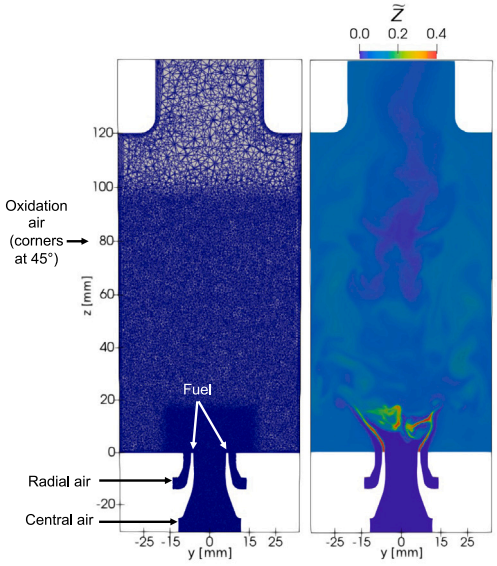


Fig. 8. Computational grid and instantaneous mixture fraction cut from the LES with FPV model.

Table 1
Operating conditions of the model combustor from Geigle et al. [40]. Only the case at 3 bar with auxiliary oxidation jets ($Q_{air,oxid}$) is considered.

Q_{fuel} (slm)	$Q_{air,central}$ (slm)	$Q_{air,ring}$ (slm)	$Q_{air,oxid}$ (slm)	ϕ_g (-)
39.3	140.8	328.5	187.4	0.86

Instantaneous and average soot volume fraction fields collected with Laser Induced Incandescence (LII) are available, thus making it a suitable case to assess the spatial distribution of soot. Among the available operating points [40], the case at 3 bar with auxiliary air jets has been selected for this study, due to the focus on soot oxidation. The operating conditions are reported in Table 1. A more detailed description of the combustor geometry and of all the different cases available for this configuration can be found in Refs. [40,43].

A minimally-dissipative low-Mach number solver for reacting flow integrated in OpenFOAM [47] is used to perform LES. Detailed description of the numerical framework, validation of the solver, and its application for LES of the same combustor are found in Refs. [43–45,47]. The gas-phase combustion is described using either the FPV or SMLD models (Sections 2.3.1 and 2.3.2). The general conserved scalar transport equation is

$$\frac{\partial \rho\psi}{\partial t} + \frac{\partial \rho u_j \psi}{\partial x_j} = \frac{\partial}{\partial x_j}\left(\rho D_\psi \frac{\partial \psi}{\partial x_j}\right) + \rho S(\psi), \tag{24}$$

with $\psi = \{Z, C, Y_{\mathrm{PAH}}\}$ as the set of transported scalars, u_j as the velocity, D_ψ as the diffusivity of the scalar, and $S(\psi)$ as the scalar source term. The equations are filtered for LES, resulting in unclosed terms. The additional transport equation for the lumped PAH mass fraction (Y_{PAH}), its source term, and the unclosed terms due to filtering are modeled according to Mueller and Pitsch [15].

Steady one-dimensional flamelets with unity Lewis number are precomputed and tabulated. Here, the full version of the detailed kinetic model [38] used in the DNS (Section 3) is employed, since no mechanism reduction is required. Thus, detailed PAH chemistry up to 4-ring species is included.

The soot moment transport equation (Eq. (4)) is filtered as in [15] and solved for $\overline{M}_{0,0}$, $\overline{M}_{1,0}$, $\overline{M}_{0,1}$, $\overline{N}_0$ and $\overline{M}^2_{0,0}$, with the last term required for the evaluation of the soot intermittency ω used in the soot subgrid models described in Section 2.2. For the tabulation of the filtered source terms, $\widetilde{S}(\psi)$, obtained from the filtering of Eq. (24), a look-up table with $[200 \times 50 \times 25]$ points in $[\widetilde{Z}, \widetilde{C}, \widetilde{Z''^2}]$ is used for the FPV approach. An additional 15 points for $\widetilde{C''^2}$ are employed for the SMLD model (Eq. (21)). Subgrid mixture fraction and progress variable variances ($\widetilde{Z''^2}$ and $\widetilde{C''^2}$) are calculated algebraically.

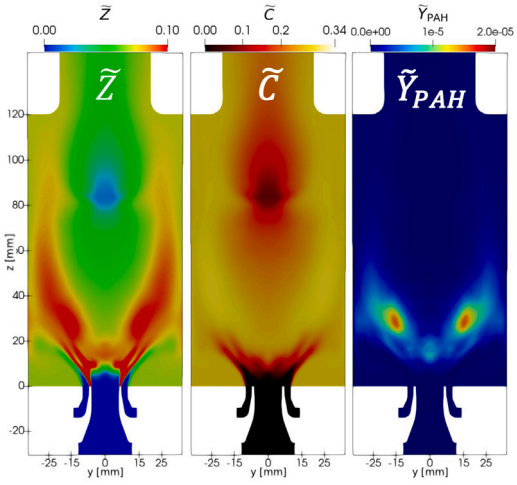


Fig. 9. Time-averaged fields from LES with FPV. Left: mixture fraction $\langle\widetilde{Z}\rangle$, center: progress variable $\langle\widetilde{C}\rangle$, right: lumped PAH mass fraction $\langle\widetilde{Y}_{\mathrm{PAH}}\rangle$.

In the following, three different cases are evaluated: FPV model paired with marginal PDF model (Eq. (10)), FPV model paired with Finite-Rate Oxidation conditional PDF model (Eq. (14)), and SMLD model (Eq. (21)) paired with marginal PDF model. Differently from the *a priori* testing, here an adaptive cut-off mixture fraction Z_{soot} is chosen, following the original model from Maldonado Colmán et al. [17], as the considered setup is not expected to have strong soot break-through or significant oxidation events in leaner regions. As in Section 3, the three models will be referred to simply as FPV, FPV-FRO, and SMLD.

4.2. Results

Average data were collected for 400 ms, which is sufficient for statistical convergence of soot fields according to Chong et al. [44]. Time-averaged mixture fraction $\langle\widetilde{Z}\rangle$, progress variable $\langle\widetilde{C}\rangle$, and lumped PAH mass fraction $\langle\widetilde{Y}_{\mathrm{PAH}}\rangle$ from the LES with only the FPV model are shown in Fig. 9. The same average fields for all three LES subgrid models are included in Section 2.1 of the supplementary material, with no significant variations observed except for a slight reduction of PAH when using the SMLD model instead of the FPV-based models.

A reasonable agreement with previous numerical studies [44–46] is observed, with the largest PAH concentration located in the two higher mixture fraction pockets near the shear layers at $z \approx 30$ mm. The main difference in the presented LES with other studies available in literature (e.g., [42,44,45]) is observed in the PAH and mixture fraction fields along the central axis near the main air inlet ($z < 20$ mm), with slightly richer mixture and significantly lower PAH concentrations. The peak PAH mass fraction is reduced by more than a factor of two compared to Chong et al. [44,45]. However, as discussed in various studies of the same setup, PAH and soot predictions, especially near the inlets, are sensitive to temperature and velocity field variations [42,44,46]. Moreover, PAH and soot concentrations vary significantly depending on the chosen kinetic model, as shown by a subsequent study from Chong et al. [45], where a different spatial soot distribution and a factor of four in peak soot volume fractions were observed when comparing two different models using the same framework.

Although the PAH concentration discrepancy along the central axis impacts the overall soot predictions compared to the experiments and

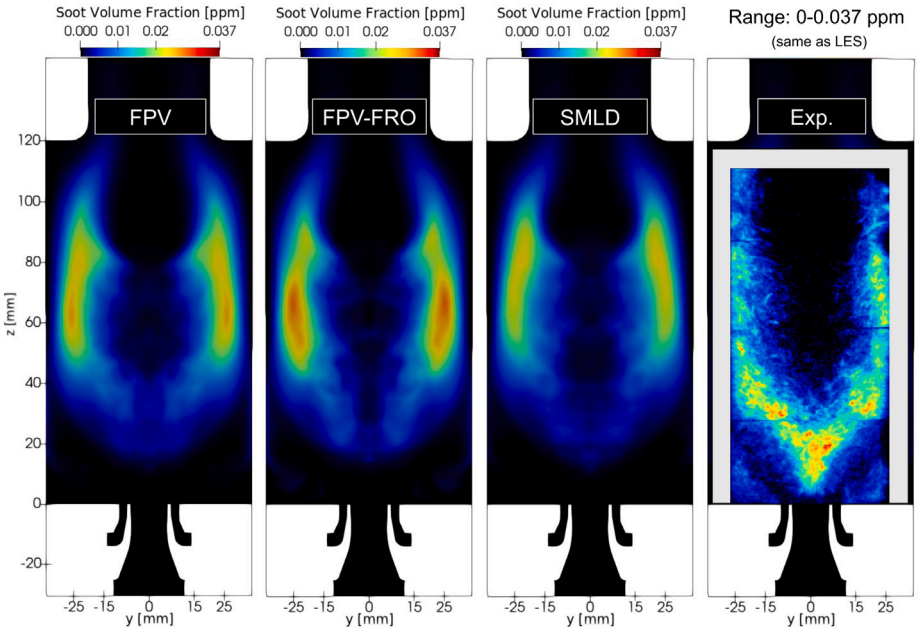


Fig. 10. Time-averaged soot volume fraction from LES (FPV, FPV-FRO, and SMLD models) and from experimental measurements from Geigle et al. [40]. The same range (0–0.037 ppm) is used for both LES and experiments.

to other studies, the model comparison presented in this section is not significantly affected, as the model difference is mainly limited to the modeling of soot oxidation (and soot surface growth by HACA for the FPV-FRO model [17]). A comparison of the time-averaged soot volume fraction spatial distribution for the three models and for the experimental counterpart from Geigle et al. [40] is presented in Fig. 10. The same data range is used for both LES and experiments. A consistent underprediction of soot volume fraction, compared to the experiment, is observed in the main soot inception and PAH adsorption region near the inlets, due to the lower PAH prediction above the main air inlet. The average fields for the three considered combustion closures appear similar, both qualitatively and quantitatively, except for a slight reduction in peak soot volume fraction for the SMLD case. The PAH dimer production term $\dot{\omega}_{\text{Dimer}}$, here modeled as by Mueller et al. [14], has been shown to have significant variability in a narrow progress variable range [48], thus small variations to the progress variable source term ($\dot{\omega}_C$) introduced with the SMLD model sensibly impact the PAH and soot distributions (see Section 2.1 of the supplementary material for the average PAH fields). Conversely, HACA and oxidation rate constant distributions are typically wider in the Z-C space [48], thus small variation in C have a much smaller impact on the average fields. Compared to canonical jet flames, this model combustor configuration has been shown to exhibit stronger acetylene-based soot growth [44]. Here, the largest bulk of soot is located in the lateral wings (similar to Ref. [46]), suggesting an HACA-growth overprediction which compensates the lower PAH-based formation and growth observed for all cases. By definition, the FRO model uses the prescribed cut-off value Z_{soot} for both the oxidation and HACA growth rates (k_{Ox} and k_{HACA}), since applying the model only to oxidation would lead to unrealistic growth rates below Z_{soot} not counteracted by any oxidation. Nonetheless, except for a slight variation in distribution between FPV and FPV-FRO in the downstream wings, where HACA growth is predominant, no significant change is observed, implying that the results would not be impacted with a more conservative fixed cut-off mixture fraction (as for the *a priori* analysis) for the FPV-FRO model.

To assess the capability of the three different models in capturing soot break-through, i.e., presence of soot in lean regions, a comparison of the scatter plots of soot volume fraction against mixture fraction

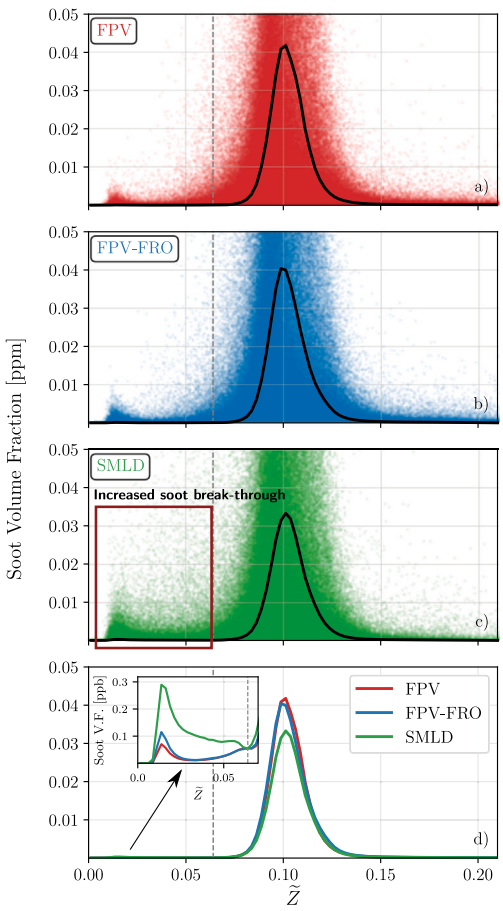


Fig. 11. Soot volume fraction conditioned on mixture fraction with scatter plot. Data averaged using 2000 cut planes across 400 ms of simulation time. (a): FPV, (b): FPV-FRO, (c): SMLD, (d) Comparison of the three cases. Inset: detail of soot volume fraction conditional mean below stoichiometry (in ppb, factor of ≈100 compared to main plot).

is given in Fig. 11. The data are collected from 2000 snapshots of the central plane, across the full 400 ms of simulation time. Although the combustor configuration is globally lean and exhibits no strong smoking behavior, some soot is observed below stoichiometry for all cases. The most soot break-through, both in occurrences and amount, is observed for the SMLD model; significantly more data, with moderately large values, are found way below the main oxidation range ($\widetilde{Z} < 0.05$), most probably as a result of soot break-through due to local reduction in oxidation rates (i.e., partial or complete local extinction). In Fig. 11d, the three conditional means are compared, where the detailed inset shows the soot distribution below stoichiometry. In this region, while the overall soot levels are significantly lower than in the main soot formation and growth region (by roughly two orders of magnitude below peak values), SMLD predicts a threefold increase in leaked soot volume fraction compared to FPV/FPV-FRO. While the soot distribution above stoichiometry appear similar across models, the increased lean-region soot predicted by SMLD — attributed to soot break-through — suggests a significant increase in total combustor emissions. Moreover, the SMLD model does not require any prescribed cut-off value, which could affect the average acetylene-based growth and oxidation rates. In conclusion, the LES results show that, while modest, soot break-through events can occur even under globally lean conditions, as shown in previous DNS works [6,7], due to soot-turbulence-chemistry interactions. This is mainly due to soot crossing locally extinct flame regions, and not due to a gradual, incomplete oxidation of soot through the oxidation layers. It should be noted that this interpretation of the LES results is primarily inferred from the *a priori* analysis of the DNS data exhibiting strong break-through, as the available experimental data do not allow for direct validation of soot break-through occurrences. This assessment could be strengthened by further validation under strongly sooting conditions with significant extinction. However, other turbulent flame experiments, even those in which soot break-through has been observed (e.g., Ref. [9]), typically use diluted fuels or strongly oxidizing conditions to avoid excessive smoke production, which would otherwise interfere with optical measurements. Thus, to fully assess the impact of soot break-through on global emissions, further studies on heavily sooting turbulent flames are needed. The presented work demonstrates that the SMLD model can capture soot break-through and secondary oxidation events well, thus being a suitable candidate for such conditions.

5. Conclusions

The modeling of soot oxidation in non-premixed turbulent flames under soot break-through conditions was explored in this work. Three reduced-order models were assessed both *a priori* and *a posteriori*, to evaluate their accuracy under strong extinction conditions and their capability in capturing soot break-through events (i.e., soot reaching lean mixtures without complete oxidation). The baseline reduced-order model employs an FPV approach and a 2δ presumed PDF model for the soot subfilter distribution, assuming a time scale separation of soot and gas-phase. The second model uses the same FPV approach and extends the 2δ approach to account for fast soot evolution processes such as soot oxidation, including effects of finite-rate soot oxidation (FRO) events with a cut-off mixture fraction Z_{soot} in the presumed conditional PDF of soot and gas-phase. The third model is a Statistically Most Likely Distribution (SMLD) model, coupled with the original 2δ approach for soot (hence, the soot/gas-phase time scale separation). The SMLD model is an extended version of the FPV model, which, by using higher-order moment information for the progress reaction parameter, has been shown to improve local extinction and reignition predictions. Here, for the first time, the SMLD approach was applied to model soot oxidation rates.

The models were tested *a priori* against DNS data characterized by strong local extinctions and significant soot break-through. The SMLD model was shown to improve the filtered soot oxidation rate predictions under soot break-through conditions, especially in lean regions where secondary oxidation occurs due to unsteady extinction and reignition effects. Conversely, the FPV-FRO model significantly underpredicts these events, as its formulation assumes little to no oxidation below the prescribed cut-off value, typically set at stoichiometry or above. As soot break-through is marginally sensitive to the actual oxidation rates and mainly linked to local extinction, the improvement shown by the SMLD model are expected to be robust with respect to oxidation kinetic variations.

Then, the models were tested *a posteriori* in LES of a high-pressure swirl combustor with secondary oxidation air jets. While the baseline case underpredicts soot formation along the central axis near the inlets, a reasonable spatial distribution of soot compared to the experiments was observed, allowing comparisons of the different soot oxidation models. The three models exhibited similar average soot volume fraction distribution. However, increased concentrations of soot in the lean regions were observed for the SMLD model, indicating more soot break-through events, due to local extinctions (even under globally lean conditions). Such a difference in soot break-through prediction could translate into significantly different levels of engine-out soot emissions in practical gas turbine applications. Further evaluations on strongly sooting flames with substantial extinctions are suggested to better assess the impact of soot break-through on global soot emissions.

Overall, the SMLD model applied to soot oxidation has been shown to capture soot break-through, and to improve secondary soot oxidation predictions in the leaner regions due to partial extinctions and reignitions, without introducing any dependency of soot on the mixture fraction. Moreover, the SMLD model can be employed with good generalizability to different conditions (e.g., fuel or pressure), as the model basically introduces a modified reaction progress parameter PDF only in the regions where soot break-through or secondary oxidation might occur, based on a chemistry/flow time scale ratio.

CRediT authorship contribution statement

Gandolfo Scialabba: Writing – review & editing, Writing – original draft, Methodology, Investigation, Formal analysis, Data curation, Conceptualization. **Kai Niemietz:** Writing – review & editing, Conceptualization. **Antonio Attili:** Writing – review & editing, Conceptualization. **Heinz Pitsch:** Writing – review & editing, Supervision, Project administration, Funding acquisition, Conceptualization.

Declaration of competing interest

The authors declare that they have no known competing financial interests or personal relationships that could have appeared to influence the work reported in this paper.

Acknowledgments

Generous support of the Deutsche Forschungsgemeinschaft (DFG, German Research Foundation) under grant number 434872808 and the FVV e.V. under grant number 6015040 is gratefully acknowledged. The authors gratefully acknowledge the Gauss Centre for Supercomputing e.V. (www.gauss-centre.eu) for funding this project by providing computing time on the GCS Supercomputer HAWK at Höchstleistungsrechenzentrum Stuttgart (www.hlrs.de). The authors wish to thank Prof. Venkat Raman and his group for providing the LES code used for *a posteriori* testing, Dr. Klaus Peter Geigle for providing the experimental data for the model combustor, and Geveen Arumapperuma for providing the computational grid for the simulations. The data used in this publication was managed using the research data management platform Coscine (DOI) with storage space of the Research Data Storage (RDS) (DFG: INST222/1261-1) and DataStorage.nrw (DFG: INST222/1530-1) granted by the DFG and Ministry of Culture and Science of the State of North Rhine-Westphalia.

Appendix A. Supplementary data

Supplementary material including additional statistics for the results presented is associated with this article.

Supplementary material related to this article can be found online at https://doi.org/10.1016/j.combustflame.2026.115085.

References

[1] V. Raman, R.O. Fox, Modeling of fine-particle formation in turbulent flames, Ann. Rev. Fluid Mech. 48 (2016) 159–190.

[2] D.O. Lignell, J.H. Chen, P.J. Smith, Three-dimensional direct numerical simulation of soot formation and transport in a temporally evolving nonpremixed ethylene jet flame, Combust. Flame 155 (2008) 316–333.

[3] F. Bisetti, G. Blanquart, M.E. Mueller, H. Pitsch, On the formation and early evolution of soot in turbulent nonpremixed flames, Combust. Flame 159 (2012) 317–335.

[4] A. Attili, F. Bisetti, M.E. Mueller, H. Pitsch, Formation, growth, and transport of soot in a three-dimensional turbulent non-premixed jet flame, Combust. Flame 161 (2014) 1849–1865.

[5] A. Attili, F. Bisetti, M.E. Mueller, H. Pitsch, Damköhler number effects on soot formation and growth in turbulent nonpremixed flames, Proc. Combust. Inst. 35 (2015) 1215–1223.

[6] G. Scialabba, M. Davidovic, A. Attili, H. Pitsch, Direct numerical simulation of soot break-through in turbulent non-premixed flames, Combust. Flame 275 (2025) 114093.

[7] G. Scialabba, A. Attili, H. Pitsch, Influence of soot oxidation reaction time scale on soot break-through, Proc. Combust. Inst. 41 (2025) 105930.

[8] N. Qamar, Z. Alwahabi, Q. Chan, G. Nathan, D. Roekaerts, K. King, Soot volume fraction in a piloted turbulent jet non-premixed flame of natural gas, Combust. Flame 156 (2009) 1339–1347.

[9] S. Kruse, J. Ye, Z. Sun, A. Attili, B. Dally, P. Medwell, H. Pitsch, Experimental investigation of soot evolution in a turbulent non-premixed prevaporized toluene flame, Proc. Combust. Inst. 37 (2019) 849–857.

[10] Y. Wang, S.H. Chung, Soot formation in laminar counterflow flames, Prog. Energ. Combust. 74 (2019) 152–238.

[11] N. Peters, Turbulent Combustion, Cambridge University Press, 2000.

[12] J.H. Kent, H.G. Wagner, Why do diffusion flames emit smoke, Combust. Sci. Technol. 41 (1984) 245–269.

[13] P. Narayanan, A. Trouvé, Radiation-driven flame weakening effects in sooting turbulent diffusion flames, Proc. Combust. Inst. 32 (2009) 1481–1489.

[14] M.E. Mueller, H. Pitsch, Large eddy simulation subfilter modeling of soot-turbulence interactions, Phys. Fluids 23 (2011) 115104.

[15] M.E. Mueller, H. Pitsch, LES model for sooting turbulent nonpremixed flames, Combust. Flame 159 (2012) 2166–2180.

[16] S. Yang, J.K. Lew, M.E. Mueller, Large eddy simulation of soot evolution in turbulent reacting flows: Presumed subfilter PDF model for soot–turbulence–chemistry interactions, Combust. Flame 209 (2019) 200–213.

[17] H. Maldonado Colmán, A. Attili, M.E. Mueller, Large eddy simulation of turbulent nonpremixed sooting flames: Presumed subfilter PDF model for finite-rate oxidation of soot, Combust. Flame (2023) 112602.

[18] M. Ihme, H. Pitsch, Prediction of extinction and reignition in nonpremixed turbulent flames using a flamelet/progress variable model: 1. a priori study and presumed PDF closure, Combust. Flame 155 (2008) 70–89.

[19] M. Ihme, H. Pitsch, Prediction of extinction and reignition in nonpremixed turbulent flames using a flamelet/progress variable model: 2. Application in LES of sandia flames d and e, Combust. Flame 155 (2008) 90–107.

[20] C.D. Pierce, P. Moin, Progress-variable approach for large-eddy simulation of non-premixed turbulent combustion, J. Fluid. Mech. 504 (2004) 73–97.

[21] R. Barlow, J. Frank, A. Karpetis, J.-Y. Chen, Piloted methane/air jet flames: Transport effects and aspects of scalar structure, Combust. Flame 143 (2005) 433–449.

[22] M. Frenklach, Method of moments with interpolative closure, Chem. Eng. Sci. 57 (2002) 2229–2239.

[23] Ü.Ö. Köylü, G.M. Faeth, T.L. Farias, M.d.G. Carvalho, Fractal and projected structure properties of soot aggregates, Combust. Flame 100 (1995) 621–633.

[24] M.E. Mueller, G. Blanquart, H. Pitsch, A joint volume-surface model of soot aggregation with the method of moments, Proc. Combust. Inst. 32 (2009) 785–792.

[25] M. Frenklach, D.W. Clary, W.C. Gardiner Jr., S.E. Stein, Detailed kinetic modeling of soot formation in shock-tube pyrolysis of acetylene, Symp. (Int.) Combust. 20 (1985) 887–901.

[26] R. Santoro, T. Yeh, J. Horvath, H. Semerjian, The transport and growth of soot particles in laminar diffusion flames, Combust. Sci. Technol. 53 (1987) 89–115.

[27] M. Mueller, G. Blanquart, H. Pitsch, Hybrid method of moments for modeling soot formation and growth, Combust. Flame 156 (2009) 1143–1155.

[28] M.E. Mueller, Large eddy simulation of soot evolution in turbulent reacting flows (Ph.D. thesis), Stanford University, 2012.

[29] K. Neoh, J. Howard, A. Sarofim, Soot oxidation in flames, in: Particulate Carbon, Springer, 1981, pp. 261–282.

[30] G. Blanquart, Chemical and statistical soot modeling (Ph.D. thesis), Stanford University, 2008.

[31] A. Kazakov, H. Wang, M. Frenklach, Detailed modeling of soot formation in laminar premixed ethylene flames at a pressure of 10 bar, Combust. Flame 100 (1995) 111–120.

[32] H. Pitsch, Large-eddy simulation of turbulent combustion, Annu. Rev. Fluid Mech. 38 (2006) 453–482.

[33] H. Guo, P.M. Anderson, P.B. Sunderland, Optimized rate expressions for soot oxidation by OH and o_2, Fuel 172 (2016) 248–252.

[34] N. Peters, Laminar diffusion flamelet models in non-premixed turbulent combustion, Prog. Energy Combust. Sci. 10 (1984) 319–339.

[35] A.W. Cook, J.J. Riley, A subgrid model for equilibrium chemistry in turbulent flows, Phys. Fluids 6 (1994) 2868–2870.

[36] M. Ihme, C.M. Cha, H. Pitsch, Prediction of local extinction and re-ignition effects in non-premixed turbulent combustion using a flamelet/progress variable approach, Proc. Combust. Inst. 30 (2005) 793–800.

[37] S. Pope, A rational method of determining probability distributions in turbulent reacting flows, J. Non-Equilib. Thermodyn. 4 (1979) 309–320.

[38] R. Langer, Q. Mao, H. Pitsch, A detailed kinetic model for aromatics formation from small hydrocarbon and gasoline surrogate fuel combustion, Combust. Flame 258 (2023) 112574.

[39] A. Attili, F. Bisetti, M.E. Mueller, H. Pitsch, Effects of non-unity lewis number of gas-phase species in turbulent nonpremixed sooting flames, Combust. Flame 166 (2016) 192–202.

[40] K.P. Geigle, M. Köhler, W. O'Loughlin, W. Meier, Investigation of soot formation in pressurized swirl flames by laser measurements of temperature, flame structures and soot concentrations, Proc. Combust. Inst. 35 (2015) 3373–3380.

[41] International sooting flame (ISF) workshop – data – turbulent flames, 2020, available at URL https://www.adelaide.edu.au/cet/isfworkshop/data-sets/turbulent/.

[42] A. Wick, F. Priesack, H. Pitsch, Large-eddy simulation and detailed modeling of soot evolution in a model aero engine combustor, ASME Turbo Expo 2017 (2017).

[43] H. Koo, M. Hassanaly, V. Raman, M.E. Mueller, K. Peter Geigle, Large-eddy simulation of soot formation in a model gas turbine combustor, J. Eng. Gas Turbines Power 139 (2017) 031503.

[44] S.T. Chong, M. Hassanaly, H. Koo, M.E. Mueller, V. Raman, K.-P. Geigle, Large eddy simulation of pressure and dilution-jet effects on soot formation in a model aircraft swirl combustor, Combust. Flame 192 (2018) 452–472.

[45] S.T. Chong, V. Raman, M.E. Mueller, P. Selvaraj, H.G. Im, Effect of soot model, moment method, and chemical kinetics on soot formation in a model aircraft combustor, Proc. Comb. Inst. 37 (2019) 1065–1074.

[46] G. Arumapperuma, Y. Tang, A. Attili, W. Han, Spectral analysis of soot dynamics in an aero-engine model combustor, Proc. Combust. Inst. 40 (2024) 105344.

[47] M. Hassanaly, H. Koo, C.F. Lietz, S.T. Chong, V. Raman, A minimally-dissipative low-mach number solver for complex reacting flows in openFOAM, Comput. Fluids 162 (2018) 11–25.

[48] A. Wick, A. Attili, F. Bisetti, H. Pitsch, DNS-driven analysis of the flamelet/progress variable model assumptions on soot inception, growth, and oxidation in turbulent flames, Combust. Flame 214 (2020) 437–449.